Observing a Volatile Organic Compound from a Geostationary Infrared Sounder: HCOOH from FengYun-4B/GIIRS

Zhao-Cheng Zeng[1]*, Bruno Franco[2], Lieven Clarisse[2], Lu Lee[3], Chengli Qi[3], and Feng Lu[3]

[1]School of Earth and Space Sciences, Peking University, Beijing 100871, China

[2]Spectroscopy, Quantum Chemistry and Atmospheric Remote Sensing (SQUARES), Université libre de Bruxelles (ULB), 1050 Brussels, Belgium

[3]Innovation Center for FengYun Meteorological Satellite, Key Laboratory of Radiometric Calibration and Validation for Environmental Satellites, National Satellite Meteorological Center, China Meteorological Administration, Beijing 100081, China

Corresponding author: Z.-C. Zeng (zczeng@pku.edu.cn)

Key Points:

- First retrieval of atmospheric HCOOH from a geostationary sounder is demonstrated
- HCOOH in fire plumes can be continuously tracked with FY-4B/GIIRS
- FY-4B/GIIRS HCOOH observations have comparable sensitivity to IASI

Abstract

Formic acid (HCOOH) is one of the most abundant volatile organic compounds (VOCs) in the Earth's atmosphere and an important source of atmospheric acidity. Here we present the first retrieval of HCOOH from a geostationary orbit using observations from the Geostationary Interferometric Infrared Sounder (GIIRS) on board FengYun-4B. The results from July 2022 to June 2023 show the monthly variation of the HCOOH distribution in Asia due to emissions from biomass burning and biogenic sources. FY-4B/GIIRS effectively tracks HCOOH enhancements from wildfires and biogenic sources both during the day and at night. Finally, inter-comparison with IASI HCOOH data shows good agreement, indicating that FY-4B/GIIRS observations have comparable sensitivity to IASI. This study is an important first step towards monitoring VOCs from geostationary infrared sounders, including the existing and future GIIRS on board the FY-4 series and the forthcoming European geostationary infrared sounder (IRS) on board Meteosat Third Generation (MTG).

Plain Language Summary

Formic acid (HCOOH) is one of the most abundant volatile organic compounds (VOCs) in the Earth's atmosphere and an important source of atmospheric acidity. Satellite observations play an indispensable role in improving our understanding of global HCOOH sources and sinks. However, existing polar-orbiting satellites that are sensitive to tropospheric HCOOH only provide up to two overpasses per day over the same spot, one during the day and one during the night. The diurnal variations of tropospheric HCOOH are therefore under-constrained to track its evolution in the lower troposphere and transport in the free troposphere. The Geostationary Interferometric Infrared Sounder (GIIRS) onboard China's FengYun-4 satellite series is the world's first geostationary hyperspectral infrared sounder. Using observations from FY-4B/GIIRS, this study presents the first retrieval of HCOOH from a geostationary satellite instrument that captures the HCOOH variation in Asia driven by biomass burning emissions and biogenic sources. In addition, FY-4B/GIIRS effectively tracks HCOOH plumes in Southeast Asia and Siberia. Finally, inter-comparison with IASI HCOOH data shows good agreement, indicating that FY-4B/GIIRS observations have comparable sensitivity to IASI. This study is an important first step towards monitoring VOCs from geostationary infrared sounders.

1 Introduction

Formic acid (HCOOH) is one of the most abundant volatile organic compounds (VOCs) in the Earth's atmosphere and an important source of atmospheric acidity. It contributes significantly to precipitation acidity by facilitating the nucleation of cloud droplets (e.g., **Andreae et al., 1988; Keene and Galloway, 1984; Keene and Galloway, 1988**). The production of HCOOH in the atmosphere is dominated by photochemical oxidation of biogenic and anthropogenic VOCs (**Millet et al., 2015**) and direct emissions from vegetation (**Keene and Galloway, 1984**), biomass and biofuel burning (**Goode et al., 2000**), and fossil fuel combustions (**Kawamura et al., 1985**). Yet, advanced global models underestimate the observed atmospheric levels of HCOOH, pointing to major gaps in our understanding of its emissions and formation mechanisms.

Over the past decade, studies have showcased the essential role of satellite observations in enhancing our understanding of global sources and sinks of HCOOH. For instance, **Stavrakou et al. (2012)** showed that a large source of HCOOH from boreal and tropical forests is misrepresented in models based on satellite observations from the Infrared Atmospheric Sounding Interferometer (IASI; **Razavi et al., 2011**). Using measurements from the same sounder, **Franco et al. (2021)** proposed an HCOOH production mechanism in which formaldehyde is efficiently converted to gaseous HCOOH via a multiphase pathway. In addition, it has been shown that the HCOOH emissions from wildfires have been largely underestimated using satellite observations (e.g., **Cady-Pereira et al. 2014; Chaliyakunnel et al., 2016; Pommier et al., 2017**).

Satellite observations of HCOOH provide global coverage from polar-orbiting nadir-looking infrared hyperspectral sounders including IASI (e.g., **Razavi et al., 2011; Franco et al., 2018**) and the Tropospheric Emission Spectrometer (TES) (e.g., **Cady-Pereira et al., 2014**). In addition, solar occultations from the limb sounders Michelson Interferometer for Passive Atmospheric Sounding (MIPAS) and Atmospheric Chemistry Experiment – Fourier Transform Spectrometer (ACE-FTS) provide measurements of the HCOOH abundance in the upper troposphere – lower stratosphere (e.g., **González Abad et al., 2009; Grutter et al., 2010**), However, existing polar-orbiting satellites that are sensitive to tropospheric HCOOH can only provide up to two overpasses per day over the same spot, with one in the daytime and the other in the nighttime. The diurnal change of tropospheric HCOOH is therefore under-constrained. Although it is relatively short-lived with a global tropospheric lifetime of 3-4 days (**Paulot et al., 2011; Stavrakou et al., 2012**), HCOOH produced or released into the free troposphere can be

transported over relatively long distances due to its slow photochemical loss (**Paulot et al., 2011**). Hence, continuous high-temporal-resolution observations of HCOOH are required to track its evolution and to characterize its intra-day variability in the troposphere.

The Geostationary Interferometric Infrared Sounder (GIIRS) onboard China's FengYun-4 satellite series is the world's first geostationary hyperspectral infrared sounder primarily designed to observe the three-dimensional distributions of atmospheric water vapor and temperature. GIIRS on board FY-4B (FY-4B/GIIRS) was launched in 2021 with an improved signal-to-noise ratio (SNR) compared to its predecessor FY-4A/GIIRS, launched in 2016 (**Yang et al., 2017**). The high spectral resolution (~0.625 cm^{-1}) and SNR of FY-4B/GIIRS have enabled 2-hourly measurements of carbon monoxide and ammonia over eastern Asia (**Zeng et al., 2023a; Zeng et al., 2023b**). Applying the optimal estimation method (OEM) on the FY-4B/GIIRS spectra, this study aims to assess for the first time the information content within spectra recorded by a geostationary sounder for retrieving diurnal HCOOH over eastern Asia. Additionally, it investigates how geostationary observations can aid in tracking the long-range transport of HCOOH in the free troposphere. The rest of this paper is organized as follows. An introduction to FY-4B/GIIRS and the observed spectra is given in **Section 2**, and the retrieval algorithm based on optimal estimation is presented in **Section 3**. The results are shown in **Section 4**, followed by discussion and conclusions in **Section 5**.

2 FY-4B/GIIRS

FY-4B/GIIRS is an infrared Fourier transform spectrometer located at an altitude of ~36,000 km above the Equator at 133° E overlooking eastern Asia. FY-4B/GIIRS scans the full region with a 2-hour measurement cycle. In total, 12 cycles are made per day starting at 0, 2, 4, …, 22h UTC before September 06, 2022, and 1, 3, 5, …, 23h UTC after. In the 2-hour measurement cycle, scanning the full region takes about 1.5 hour, followed by external spectral calibration for about 0.5 hour. At nadir, the spatial footprint on the Earth's surface has a diameter of about 12 km. FY-4B/GIIRS covers a long-wave IR band (680-1130 cm^{-1}) and a mid-wave IR band (1650-2250 cm^{-1}) with a spectral resolution of 0.625 cm^{-1}. Blackbody calibration experiments (**Li et al., 2022**) carried out before launch showed that the typical noise equivalent differential radiance (NedR) around the HCOOH absorption channel at 1105 cm^{-1} (**Figure 1(a)**) is less than 0.3 $mW/(m^2 \cdot sr \cdot cm^{-1})$, which is about 0.2K for a blackbody at 300K. **Figure 1(b)** shows examples of brightness

temperature changes in the micro-window for varying HCOOH abundances (1, 2, 4 and 8 times the a priori used in the retrieval, see Section 3). In the latter three cases, the HCOOH spectral signature exceeds the spectral noise level in FY-4B/GIIRS. A more detailed description of FY-4B/GIIRS can be found in **Zeng et al. (2023b)**. Similar to **Zeng et al. (2023a; 2023b)**, only clear-sky or near-clear-sky pixels are used for the retrieval. We adopted the level-2 cloud mask (CLM) data product from the Advanced Geostationary Radiation Imager (AGRI) onboard FY-4B to filter out cloudy pixels. After cloud filtering and excluding data with a satellite zenith angle larger than 70°, the number of observations available for an entire day is typically of approximately 100,000.

3 Retrieval algorithm based on optimal estimation

We apply the FengYun-Geostationary Atmospheric Infrared Retrieval (FY-GeoAIR) algorithm, originally developed for carbon monoxide (**Zeng et al., 2023a**), for retrieving HCOOH using FY-4B/GIIRS spectra. Here, a brief introduction to FY-GeoAIR is given with descriptions of changes necessary for the HCOOH retrieval. More details about the retrieval algorithm can be found in **Zeng et al. (2023a)** and **Zeng et al. (2023b)**. Essentially, FY-GeoAIR consists of a forward radiative transfer model (RTM) for simulating upwelling radiation in the thermal infrared and an OEM-based inverse model for retrieving atmospheric parameters. In the forward RTM, the upwelling radiance has four major components: the upwelling surface thermal emission, the upwelling atmospheric thermal emissions, the surface-reflected downwelling atmospheric thermal emission, and the solar radiation from surface reflection (**Clough et al., 2006**; **Hurtmans et al., 2012**). Under clear sky conditions, scattering by clouds and aerosols can be ignored. In the forward model, surface parameters (surface skin temperature and surface pressure) and atmospheric parameters (temperature, H_2O, and ozone profiles) are extracted from the European Centre for Medium-Range Weather Forecasts (ECMWF) Reanalysis v5 (ERA5; **Hersbach et al., 2020**). The a priori HCOOH profiles over land and ocean are adopted from an updated version of the IASI a priori (**Franco et al. 2018)**, as shown in **Figure S1(a)**. The absorption coefficients for gas absorption are pre-calculated as look-up tables based on the Line-By-Line Radiative Transfer Model (LBLRTM v12.11; **Clough et al., 2005**). FY-GeoAIR retrieves the atmospheric layers below 200 hPa. In the inverse model, the retrieval algorithm searches for a solution $\boldsymbol{x}$ that minimizes the following cost function **(Rodgers, 2000)**:

$$J(\boldsymbol{x}) = [\boldsymbol{y} - \mathbf{F}(\boldsymbol{x}, \boldsymbol{b})]^T \mathbf{S}_{\boldsymbol{\varepsilon}}^{-1} [\boldsymbol{y} - \mathbf{F}(\boldsymbol{x}, \boldsymbol{b})] + (\boldsymbol{x} - \boldsymbol{x}_a)^T \mathbf{S}_a^{-1} (\boldsymbol{x} - \boldsymbol{x}_a) \quad (1)$$

where $\boldsymbol{x}$ is the state vector to be retrieved, which includes a set of parameters, including HCOOH profile, H_2O profile, column scale factors for other interfering gases (ozone, carbon dioxide, methanol, ammonia, and CFC-12), surface skin temperature, and scale factor for the atmospheric temperature profile. $\boldsymbol{y}$ is the spectral radiance observation of the micro-window (1090-1120 cm^{-1}) for retrieval; **F** represents the forward RTM; $\boldsymbol{b}$ is a set of model parameters not to be retrieved, such as observation geometries. $\mathbf{S}_{\boldsymbol{\varepsilon}}$ is the measurement error covariance matrix; $\boldsymbol{x}_a$ is the a priori state vector; $\mathbf{S}_a$ is the a priori covariance matrix for the state vector. The instrument noise (NedR) for each spectral channel is used as the measurement noise for calculating $\mathbf{S}_{\boldsymbol{\varepsilon}}$. Different from **Zeng et al. (2023b)**, the spectral noise is not enlarged to force the reduced χ^2 from the cost function to be close to 1. The Levenberg-Marquardt modification of the Gauss-Newton method is used to find the solution for the cost function (**Rodgers, 2000)**. The one-sigma variability in the a priori HCOOH profile from model simulations is about 70%, which is enlarged by a factor of 5 for calculating $\mathbf{S}_a$ to relax the a priori constraint, as shown in **Figure S1(b)**.

As described by **Rodgers (2000)**, the Degree of Freedom for Signal (DOFS) and Averaging Kernel (AK) matrix, two statistics generated from OEM, can be used to interpret the retrieval results. AK is a metric that quantifies the sensitivity of the retrieval to the true state. Ideally, a sufficiently good sensitivity of an observing system generates an AK close to an identity matrix. In reality, due to the limited detectivity of the observing system, the AK can be very different. In this case, the rows of AK represent the smoothing functions that vertically smooth the information from the true state over different layers. DOFS is defined as the trace of the AK matrix, which represents the number of independent information from the spectra for constraining the vertical distribution of HCOOH. For example, a DOFS of 1.0 means that, given the assumed a priori uncertainty, one independent piece of information from the spectral can be used to constrain HCOOH vertically.

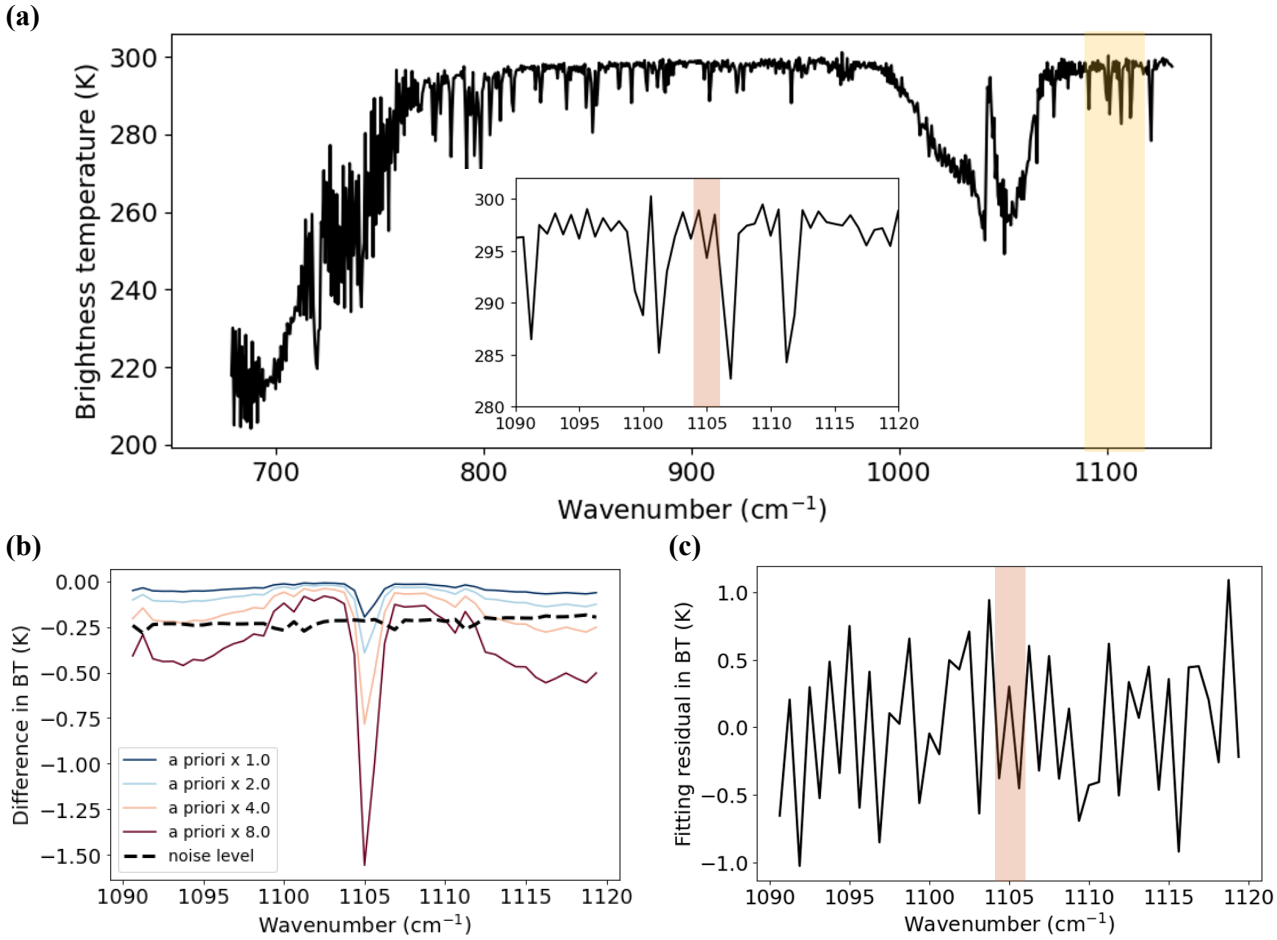

Figure 1. FY-4B/GIIRS observation spectra and the spectral window for HCOOH retrieval. (a) Example of measured longwave spectra in brightness temperature (BT) covering the HCOOH absorption micro-window centred around 1090−1120 cm^{-1}, indicated by the rectangle inset. The micro-window covers the strong absorption features of the HCOOH *v6* vibrational-rotational band; (b) Sensitivity experiment comparing absorptions of different HCOOH abundances in the 1090−1120 cm^{-1} micro-window. The difference in BT is relative to spectra without HCOOH. The simulated spectra are generated using four different HCOOH abundances based on the a priori profile with a total column of 3.1×10^{15} molec/cm^2; the simulation is based on an observation at noon time on 11 April 2023 with thermal contrast of 13K. The noise level is derived from the spectral noise estimate in the FY-4B/GIIRS data product. (c) The spectral fit residual in BT averaged over all post-filtered retrievals on the 15th of all months from July 2022 to June 2023. The filters include DOFS>0.3 and the fitting residual rmse less than the monthly mean plus two sigma The standard deviations of the fitting errors are consistent across the different channels, which is about 0.4 K. The light-red band indicates the strong HCOOH absorption between 1104 and 1106 cm^{-1}.

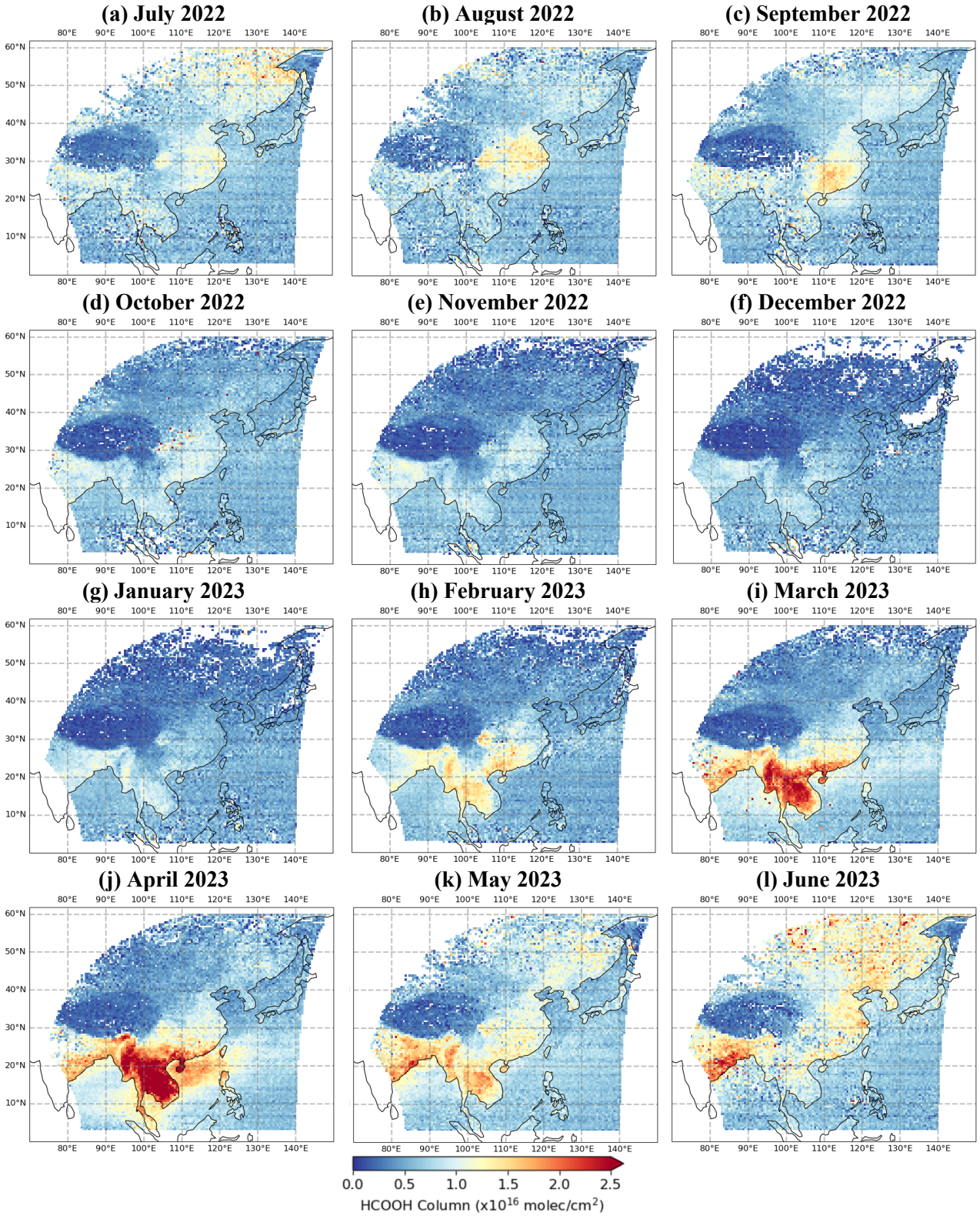

Figure 2. Monthly mean of HCOOH column retrievals at 13:00–15:00 Beijing time. These HCOOH retrievals are filtered by DOFS>0.3 and the fitting residual rmse less than the mean plus two sigma, and then gridded in 0.5° by 0.5°.

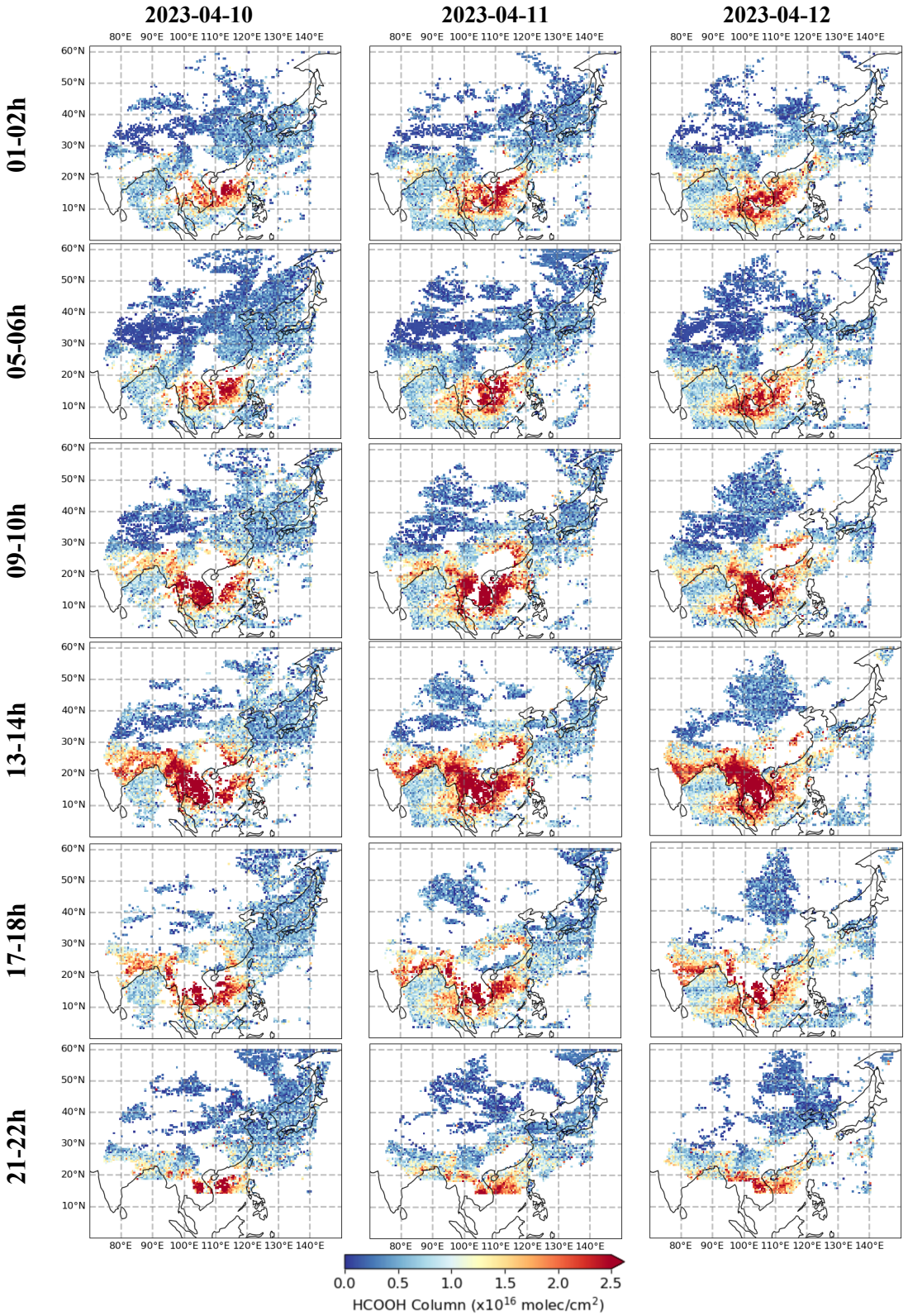

Figure 3. Example of HCOOH retrievals in each 2-hour measurement cycle from early morning to late evening on 10-12 June 2023. The data have been filtered by DOFS>0.3 and the fitting residual rmse less than the mean plus two sigma, and then gridded in 0.5° by 0.5°.

4 Results

4.1 HCOOH column retrievals and the information content

Retrieval outputs for each HCOOH observation include the HCOOH column derived from the retrieved profile, the associated posterior error covariance, the AK matrix and resulting DOFS, and the root-mean-square-error (RMSE) of the spectral fitting residual. The histograms of the fitting residual RMSE are shown in **Figures S2**. The fitting residual RMSE for all retrievals is about 0.7K on average with a standard deviation of about 0.1K. The spectral fitting residuals are shown in **Figure 1(c)**, averaged over all post-filtered retrievals on the 15th of all months from July 2022 to June 2023. Although there is a systematic pattern that can be seen in the averaged fitting residual, probably due to imperfect spectroscopy or the forward radiative transfer model, this pattern is not correlated with the absorption feature of the target gas HCOOH. To ensure high quality retrievals, the HCOOH column retrievals for each month are filtered by DOFS>0.3 and the fitting residual RMSE is less than the monthly mean plus two standard deviations.

Figure 2 shows the monthly mean of the retrieved HCOOH columns after post-filtering for the 13:00–15:00 BJT measurement cycle, when the land surface temperature and DOFS are expected to be the highest during the day, from July 2022 to June 2023. The results show the monthly changes in the HCOOH distribution over Asia, which are mainly due to the seasonality of emissions from biomass burning and biogenic sources. The largest HCOOH columns are observed in Southeast Asia in March and April, when fire emissions peak from the burning of crop residues from the so-called "slash and burn" agriculture (**Li et al., 2014; Lasko et al., 2017**). By examining the relationships between IASI-observed HCOOH, biogenic emissions, and fire radiative power, **Franco et al. (2020)** suggested that in Southeast Asia the high HCOOH emissions in spring are contributed jointly from terrestrial vegetation and wildfires. The authors indicated that photochemical production by various previously-identified sources lead to a stronger HCOOH enhancement over Southeast Asia. Over these regions, the HCOOH columns exceed 2.5×10^{16} molec/cm^2, which is more than 8 times the a priori column. In addition, relatively high abundances are observed over Siberia and the surrounding regions in June and July, probably due to a

combination of wildfire emissions and biogenic related emissions, as suggested by **Stavrakou et al. (2012) and Franco et al. (2021)**.

Figures S3 and **S4** show the monthly means of HCOOH columns from, respectively, the FY-4B/GIIRS retrievals covering the observation cycles at 09:00–11:00 BJT, and the daytime overpasses (~9:30 am, local solar time) of IASI/Metop-B. Similar patterns in spatial distribution can be observed for retrievals between FY-4B/GIIRS and IASI/Metop-B. Note that the morning observations in **Figs S3 and S4** provide slightly lower abundances compared to the noontime observations (**Fig. 2**), mainly due to the weaker thermal contrast (TC) conditions at the time of the IASI overpass (**Clarisse et al., 2010**) and probably to the diurnal difference in production/loss processes as introduced in **Millet et al. (2015)**. Here, TC is defined as the temperature difference between the surface and the lower atmosphere.

The information content as quantified by the DOFS is summarized in **Figure S5**. The DOFS is about 0.5 on monthly average with a standard deviation of 0.2, indicating that about half of one piece of information is available from the spectra for HCOOH retrieval based on the retrieval algorithm settings. The DOFSs over the fire plumes detected in Southeast Asia in March-April are close to 1.0, indicating that the observations provide a stronger constraint on the retrieval of fire-induced HCOOH emissions. As expected, we found that the DOFS is closely related to the TC, which is an inherent property of thermal infrared sounding (**Clarisse et al., 2010**). Such a correlation is shown in **Figure S6** for different months. Here, TC is calculated from the retrieved surface temperature and the temperature of the bottom atmospheric layer. From the correlation plots, there is a significant positive correlation between TC and DOFS, when TC is positive. The correlation coefficients are mostly larger than 0.6. The DOFS also increases slightly when TC is more negative. A similar relationship exists for the retrieval of ammonia from FY-4B/GIIRS (**Zeng et al., 2023b**). In essence, for a given HCOOH abundance, large positive TC results in strong HCOOH absorption spectral signatures. For large negative TC, HCOOH emission spectral signatures can be detected. When TC is close to zero, corresponding to the situation where the lower atmosphere with concentrated HCOOH has a similar temperature to the surface, it is difficult

240 to decorrelate the surface layer with the rest of the lower troposphere which hampers the trace gas
241 retrieval (**Bauduin et al., 2017**).

242

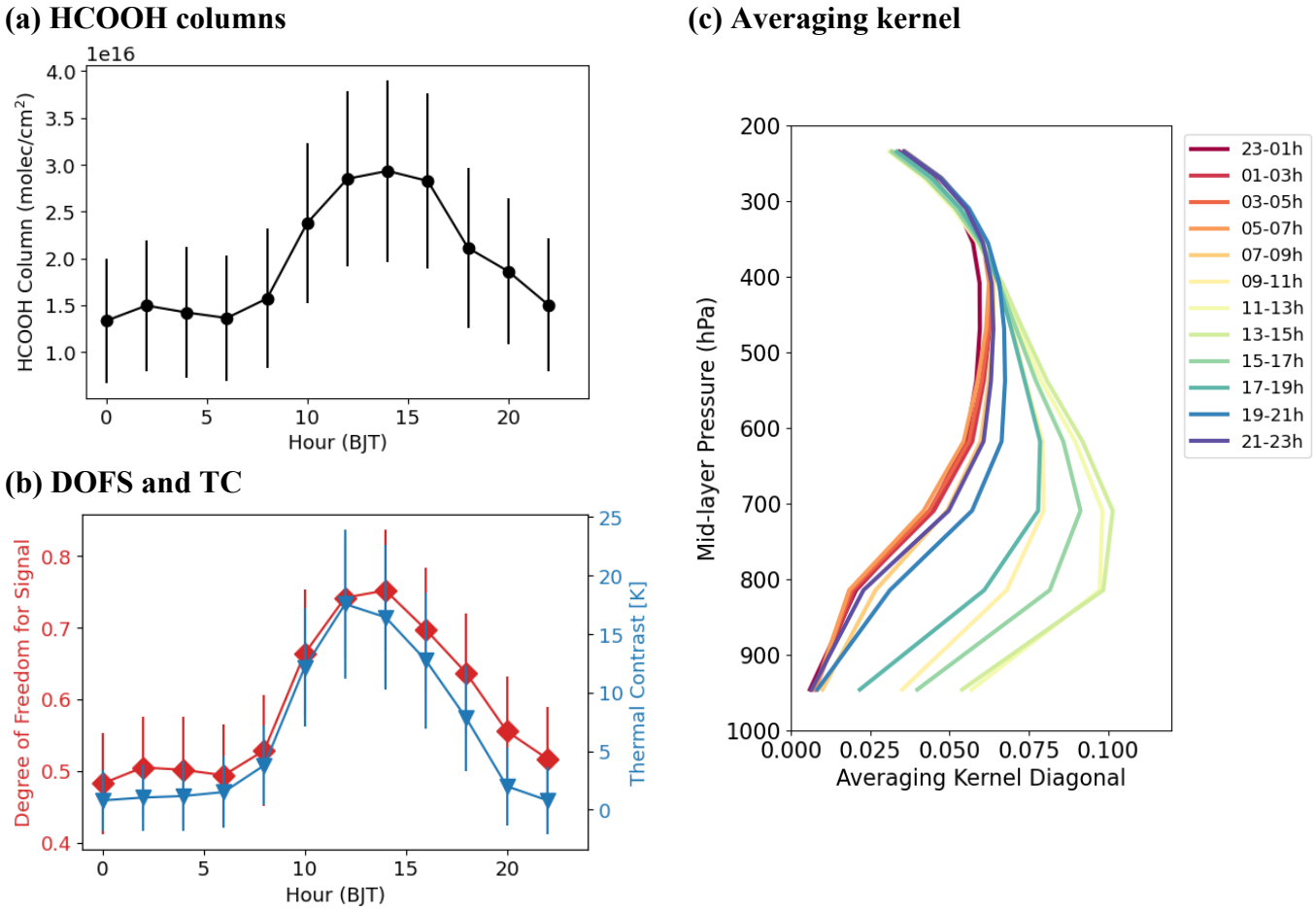

243

244 **Figure 4. The diurnal cycle in Southeast Asia. (a) Diel cycle of HCOOH columns (for every**
245 **measurement cycle of two hours) averaged for all data in April 2023 over the wildfire regions**
246 **in southeast Asia (100°E-105°E, 15°N-20°N) in the upper panel and the associated DOFS and**
247 **TC in the bottom panel. Error bars represent 1 sigma; Data have been filtered by DOFS>0.3**
248 **and the spectral fitting residual less than the sum of the mean and 2 sigma; (c) Averaged AK**
249 **diagonal vectors for every measurement cycle in April 2023 over the same region as (a)**

250

4.2 Diurnal variations of HCOOH column retrievals

FY-4B/GIIRS from the geostationary orbit has the advantage of observing at high temporal resolution in both the daytime and nighttime, allowing the characterization of the HCOOH diel cycle over East and Southeast Asia. Here, two cases are shown separately for the wildfire emissions in Southeast Asia (**Figure 3**) and the biogenic emissions in Siberia (**Figure S7**), separately. These events serve as good case studies to demonstrate the tracking capability of FY-4B/GIIRS from geostationary orbit. From Figure 3, the strong enhancement of the HCOOH columns over Southeast Asia and the transport to the surrounding oceans can be clearly observed for all day and night observations. As expected, the columns are highest in the mid-afternoon and lowest in the night. On average, the afternoon HCOOH columns, which peak around 14:00 BJT, are twice as high as the nighttime values, as shown in **Figure 4(a)**. This diurnal cycle of HCOOH columns is consistent with fire radiative power from satellite-based active fire products (**Giglio, 2007; Roberts et al., 2009**), which is associated with the diurnal changes in temperature, humidity, and human activity. Similar patterns can be seen between the daytime and nighttime overpasses of the IASI HCOOH retrievals, as shown in **Figure S8**.

However, the diel cycle detectivity of GIIRS is influenced by the diurnal variations of TC over land, as has been demonstrated for other trace gases **(Zeng et al., 2023a; 2023b)**, which affects the information content available from the observed spectra. This effect can be seen in the HCOOH retrievals from FY-4B/GIIRS, as shown in **Figure 4(b).** The diurnal cycles of the HCOOH columns and the associated DOFS and TC over the source region are highly correlated. Fortunately, when the TC is low, during the night, the DOFS is still high (on average about 0.5), providing a good constraint for the detection of HCOOH columns from the nighttime spectral measurements. As a result, the nighttime HCOOH columns ($\sim 1.5\times10^{16}$ molec/cm^2) are about 5 times larger than the a priori total column (3.1×10^{15} molec/cm^2) used in the retrieval algorithm. The change in detectivity from day to night is also reflected in the AK matrix, which indicates the sensitivity of the retrieved HCOOH partial columns in each atmospheric layer to the "truth". **Figure 4(c)** shows the averaged AK diagonal vectors, which quantify the detectivity of each layer from the observed spectra. FY-4B/GIIRS has a higher detectivity during the day than at night.

From midnight (i.e., 0h) to midday (i.e., 12h), the AK values increase, and the most sensitive layer shifts towards the lower atmosphere.

During the summer, large plumes of HCOOH can be observed in Siberia and the surrounding areas, transported over long distances from the source regions towards the east. These plumes usually escape from the boundary layer to reach the free troposphere where they undergo long-range transport (**Pommier et al., 2017; Franco et al., 2020**). One of these events in early June resulted in the formation of an elongated plume with a high HCOOH abundance, extending from central Siberia to northern China, as is shown in **Figure S7**. The propagation and dilution of the same plume of HCOOH columns can be observed from early morning to late evening on 09-11 June 2023. The retrieved columns show considerable diurnal variations. The HCOOH enhancements from the nighttime retrievals are less pronounced than those from the daytime retrievals. With a lifetime of several days in the free troposphere, significant intraday variations of the HCOOH abundance are usually not expected. However, in the case of a plume where secondary formation of HCOOH associated with photochemical production along the transport is intense, such a diurnal change may be possible. However, the change can also be partially attributed to the diel cycle of TC. Similar patterns can be seen from the IASI HCOOH retrievals, as shown in **Figure S9**.

4.3 Inter-comparison with IASI HCOOH retrievals

Independent column measurements from ground-based FTIR for validation, as in **Franco et al. (2020)**, are unfortunately not available over this region. Instead, accuracy assessment of the FY-4B/GIIRS HCOOH retrievals is performed by inter-comparison with IASI retrievals. The first generation of IASI HCOOH (**Razavi et al., 2011; Pommier et al., 2016**) was retrieved using a fast algorithm based on brightness temperature differences, which were then converted to HCOOH columns using conversion factors derived from OEM performed over source regions. A new IASI HCOOH product has been developed by **Franco et al. (2018)** using the Artificial Neural Network for IASI (ANNI) retrieval framework, which is based on machine learning and a hyperspectral range index that shows good sensitivity to the weak spectral absorption signature of HCOOH. IASI HCOOH data have been used in combination with model simulations and have significantly

improved our understanding of HCOOH sources and sinks globally (e.g., **Stavrakou et al., 2012; Pommier et al., 2016; Franco et al., 2021**).

In this study, we use the ANNI HCOOH v4 product from IASI/Metop-B and perform collocated point-by-point comparisons. A collocated point pair between GIIRS and IASI is defined as observation footprints that are less than 20 km apart in space and differ by less than 1 hour apart in observation time. Theoretically, the comparison between two different instruments need to reconcile the retrieval a priori profiles and the vertical sensitivity as quantified by the AK matrix. Both IASI and GIIRS use the same a priori profiles, which is an advantage for the comparison. In addition, **Pommier et al. (2016)** showed that the vertical sensitivity of IASI in observing HCOOH peaks between 1km and 6km, which is consistent with GIIRS as shown in **Figure 4**. Therefore, in this study, we carry out direct comparisons of HCOOH columns between GIIRS and IASI. The comparison results are shown in **Figure 5 and Figure S10** for the day and night overpasses of IASI. We specifically focus on the months when there are strong HCOOH emissions in March, April, June, and July of 2023. The correlations are analyzed for three different DOFS filters of GIIRS representing different levels of observational information content. Overall, the two datasets show good agreement, especially for the daytime observations when there is a higher TC. A persistent difference can be observed in all cases where GIIRS shows slightly higher HCOOH columns compared to IASI. The RMSE is between 4.5×10^{15} and 6.0×10^{15} molec/cm^2, which may be dominated by the retrieval uncertainty related to spectral noise. As expected, the agreement improves as the DOFS filter becomes more stringent, suggesting that part of the systematic difference is due to the lack of information content. Examples of scene-by-scene comparisons are also made that compare the re-gridded IASI retrievals (in 0.5° by 0.5° grids) in a single track with the re-gridded GIIRS retrievals from the closest measurement cycle. The retrieval noise is expected to be reduced for the gridded averages of the HCOOH columns. **Figures S11-S12** show examples of the comparison on April 10 and June 10 for scenes with significant emissions. These results show that FY-4B/GIIRS overlooking East and Southeast Asia from a geostationary orbit has comparable detectivity of HCOOH columns to IASI in the low Earth orbit.

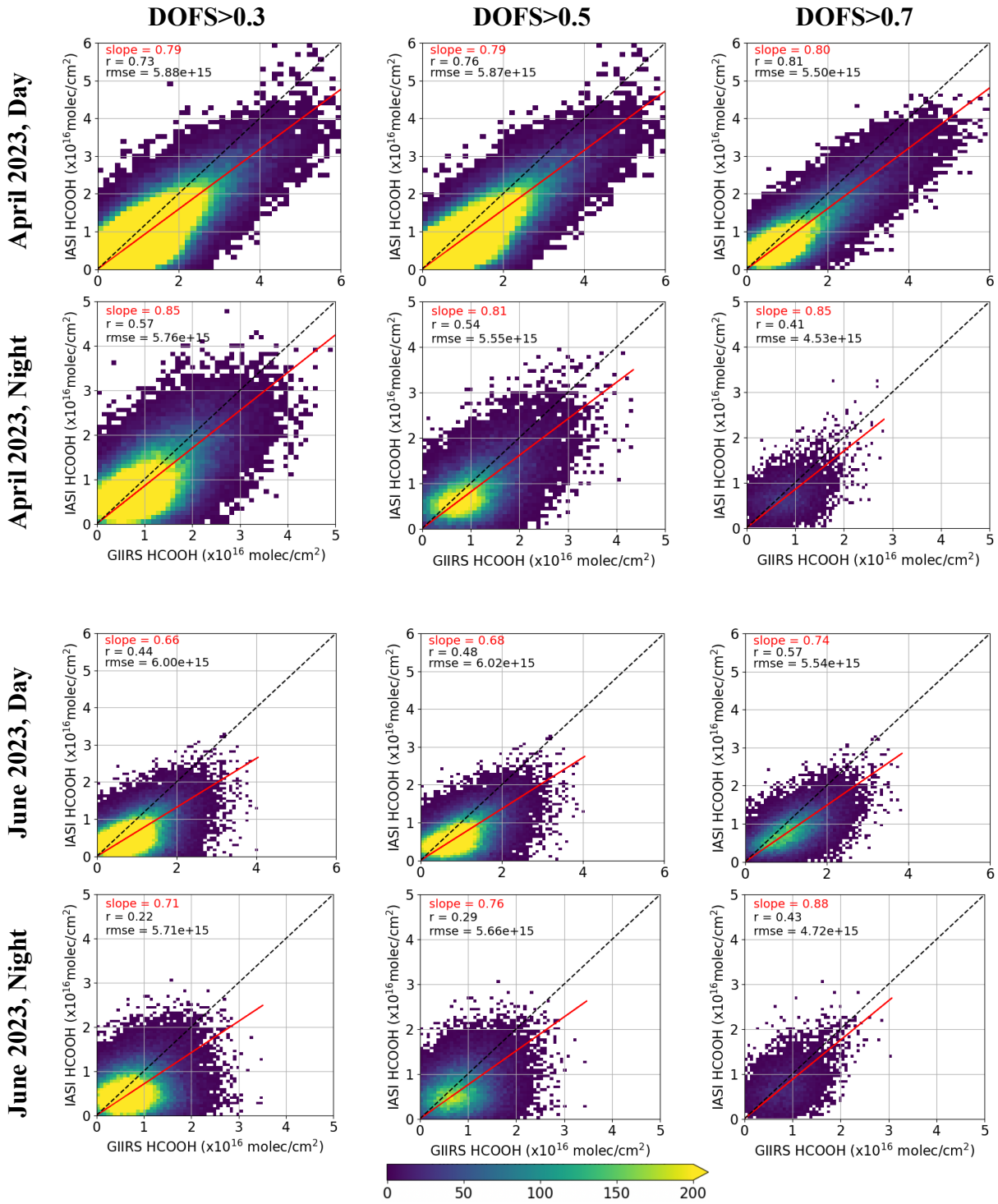

Figure 5. Comparison of HCOOH columns between GIIRS and IASI retrievals in April 2023 and June 2023, separately for day and night. Collocated point pairs are defined as observation footprints that are less than 20 km apart in space and differ by less than 1 hour in observation time. The black dashed line is the 1:1 line while the red line is the linear fit through the origin. The slope, correlation coefficient (r), and root-mean-square-error (rmse) are also given. These IASI HCOOH retrievals are filtered by the "postfilter" variable in the data product. GIIRS HCOOH retrievals are filtered by DOFS>0.3 and fitted residual rmse less than the mean plus two sigma.

5 Conclusions

This study presents the first results of retrieved atmospheric HCOOH retrieval from a geostationary orbit using infrared hyperspectral observations from FY-4B/GIIRS. By applying the FY-GeoAIR retrieval algorithm based on OEM, this study quantifies the information content of the spectra in retrieving the diurnal HCOOH over Asia from July 2022 to June 2023, and investigates how geostationary observations can facilitate continuous tracking of diurnal wildfire emissions and the long-range transport of HCOOH. Our results show that the DOFS, which represents the detectivity of HCOOH, is about 0.5 on a monthly average with a standard deviation of 0.2, indicating that about half of a piece of information from the spectra is available for HCOOH retrieval. In addition, the DOFS is closely related to the diurnal variation of TC, resulting in the highest DOFS during the day and the lowest during the night. Nevertheless, when the TC is low during the night, the DOFS is still sufficiently high to provide a constraint for the measurement of HCOOH columns from wildfire emissions. In addition, from midnight (i.e., 0h) to midday (i.e., 12h), the atmospheric layer with the highest detectivity, as indicated by the AK matrix, changes from the upper to the lower troposphere. Finally, inter-comparison with IASI HCOOH retrievals shows good agreement, indicating that FY-4B/GIIRS observations have comparable detectivity of HCOOH columns to IASI in the low Earth orbit. Ideally, GIIRS HCOOH columns should be compared with independent column measurements such as ground-based FTIR measurements, similar to **Franco et al. (2020)**. The ground-based measurements would provide a more robust validation of the GIIRS HCOOH data. There are a few FTIR stations over the GIIRS coverage area. Unfortunately, they do not provide publicly available retrievals of HCOOH.

Tracking the abundance of HCOOH is important for understanding the complex processes of HCOOH production, evolution, and loss in the atmosphere, especially for HCOOH plumes that reach the free troposphere and survive for long distances. For example, GIIRS observations with HCOOH-to-CO enhancement ratios can be used to study the secondary formation of HCOOH along a plume. FY-4B/GIIRS in the geostationary orbit provides such important information with its HCOOH retrievals every two hours from early morning to late evening. Given the diurnal change in the information content available from the observed spectra, it is important to include the AK matrix in further analysis such as data assimilation. Future work will focus on verifying chemical transport model simulations of HCOOH with satellite observations to understand the diel

372 characteristics of sources and sinks of HCOOH in Asia, especially over major source regions, and
373 to track the evolution of HCOOH in the atmosphere.

374 This study is an important first step towards monitoring VOCs from geostationary infrared
375 sounders from a constellation of geostationary infrared sounders, including the existing and future
376 GIIRS on board the FY-4 series over Asia and the forthcoming European geostationary infrared
377 sounder (IRS) on board Meteosat Third Generation (MTG) over Europe.
378

Acknowledgment

The authors would like to thank Prof. Yuk L Yung at Caltech and Prof. Yuanlong Huang at Eastern Institute of Technology, Ningbo (EIT) for stimulating discussions. Z.-C. Zeng acknowledges funding from the National Key R&D Program of China (grant no. 2022YFA1003801) and the National Natural Science Foundation of China (grant no. 42275142 and no. 12292981). This work was also supported by High-performance Computing Platform of Peking University. Research at the National Satellite Meteorological Center (NSMC) was funded by NSMC of China Meteorological Administration (CMA) under the program of Calibration Technology Development and Level-1 Data Production for the Hyperspectral Imaging and Sounding Instruments onboard FY-3E and FY-4B Satellites (FY-APP-2021.0507). IASI is a joint mission of EUMETSAT and the Centre National d'Etudes Spatiales (CNES, France). The authors acknowledge the AERIS data infrastructure for providing access to the IASI data. The research at ULB has been supported by the IASI.Flow Prodex arrangement (ESA–BELSPO). Lieven Clarisse is a research associate supported by the F.R.S.–FNRS.

Open Research

The HCOOH retrieval data from FY-4B/GIIRS in this study are available at [**https://disk.pku.edu.cn/link/AA9FDC4AD607334B718F6A21E7870837F8%20Folder%20Name:%20FY4B_GIIRS_HCOOH_v2**] and will be made publicly available upon publication. FY-4B/GIIRS Level 1 data are publicly available from the FengYun Satellite Data Center at http://satellite.nsmc.org.cn/portalsite/default.aspx; The surface emissivity datasets are downloaded from the Global Infrared Land Surface Emissivity: UW-Madison Baseline Fit Emissivity Database at https://cimss.ssec.wisc.edu/iremis/; The ECMWF ERA5 reanalysis datasets are available from the Copernicus Climate Data Store at https://cds.climate.copernicus.eu/cdsapp#!/dataset/reanalysis-era5-pressure-levels and https://cds.climate.copernicus.eu/cdsapp#!/dataset/reanalysis-era5-single-levels; The ECMWF atmospheric composition datasets are available from the Copernicus Atmosphere Data Store at https://ads.atmosphere.copernicus.eu/cdsapp#!/dataset/cams-global-atmospheric-composition-forecasts. The IASI/Metop-B HCOOH columns presented in this paper are publicly available on Zenodo (https://doi.org/10.5281/zenodo.10894008).

Competing interest

The authors declare that they have no conflict of interest.

411 **References**

412 Andreae, M. O., Andreae, T. W., Talbot, R. W., and Harriss, R. C. (1988), Formic and acetic
413 acid over the central Amazon region, Brazil. I. Dry season, *Journal of Geophysical Research*, 93,
414 1616–1624, doi:10.1029/JD093iD02p01616.

415 Bauduin, S., Clarisse, L., Theunissen, M., George, M., Hurtmans, D., Clerbaux, C., and Coheur,
416 P.-F. (2017), IASI's sensitivity to near-surface carbon monoxide (CO): Theoretical analyses and
417 retrievals on test cases, *Journal of Quantitative Spectroscopy and Radiative Transfer*, 189, 428–
418 440, https://doi.org/10.1016/j.jqsrt.2016.12.022, 2017.

419 Cady-Pereira, K. E., Chaliyakunnel, S., Shephard, M. W., Millet, D. B., Luo, M., and Wells, K.
420 C. (2014), HCOOH measurements from space: TES retrieval algorithm and observed global
421 distribution, *Atmospheric Measurement Techniques*, 7, 2297–2311, doi:10.5194/amt-7- 2297-
422 2014.

423 Chaliyakunnel, S., Millet, D. B., Wells, K. C., Cady-Pereira, K. E., and Shephard, M. W. (2016),
424 A Large Underestimate of Formic Acid from Tropical Fires: Constraints from Space-Borne
425 Measurements, *Environmental Science and Technology*, 50, 5631–5640,
426 doi:10.1021/acs.est.5b06385.

427 Clarisse, L., Shephard, M. W., Dentener, F., Hurtmans, D., Cady- Pereira, K., Karagulian, F.,
428 Van Damme, M., Clerbaux, C., and Coheur, P.-F. (2010), Satellite monitoring of ammonia: A
429 case study of the San Joaquin Valley, *Journal of Geophysical Research*, 115,
430 https://doi.org/10.1029/2009JD013291.

431 Clough, S. A., Shephard, M. W., Worden, J., Brown, P. D., Worden, H. M., Luo, M., Rodgers,
432 C. D., Rinsland, C. P. (2006), Goldman, A., and Brown, L.: Forward model and Jacobians for
433 tropospheric emission spectrometer retrievals, *IEEE Transactions on Geoscience and Remote*
434 *Sensing*, 44, 1308–1323.

435 de Gouw, J. & Farmer, D., (2021), Cloud droplets aid the production of formic acid in the
436 atmosphere, *Nature*, 593, 198-199, doi: https://doi.org/10.1038/d41586-021-01206-5.

437 Franco, B., Clarisse, L., Stavrakou, T., Müller, J.-F., Van Damme, M., Whitburn, S., et al.
438 (2018). A general framework for global retrievals of trace gases from IASI: Application to
439 methanol, formic acid, and PAN. *Journal of Geophysical Research: Atmospheres*, 123, 13,963–
440 13,984. https://doi.org/10.1029/2018JD029633

441 Franco, B., Clarisse, L., Stavrakou, T., Müller, J.-F., Taraborrelli, D., Hadji-Lazaro, J., et al.
442 (2020). Spaceborne measurements of formic and acetic acids: A global view of the regional
443 sources. *Geophysical Research Letters*, 47,
444 e2019GL086239. https://doi.org/10.1029/2019GL086239

445 Franco, B., Blumenstock, T., Cho, C., Clarisse, L., Clerbaux, C., Coheur, P.F., De Mazière, M.,
446 De Smedt, I., Dorn, H.P., Emmerichs, T. and Fuchs, H. (2021), Ubiquitous atmospheric
447 production of organic acids mediated by cloud droplets. *Nature*, 593(7858), pp.233-237.

448 Giglio, L. (2007), Characterization of the tropical diurnal fire cycle using VIRS and MODIS
449 observations. *Remote Sensing of Environment*, 108, 407–421.

450 Goode, J., Yokelson, R., Ward, D., Susott, R., Babbitt, R., Davies, M., and Hao, W. (2000),
451 Measurements of excess O_3, CO_2, CO, CH_4, C_2H_4, C_2H_2, HCN, NO, NH_3, HCOOH, CH_3COOH,
452 HCHO, and CH_3OH in 1997 Alaskan biomass burning plumes by air-borne Fourier transform
453 infrared spectroscopy (AFTIR), *Journal of Geophysical Research*, 105, 22147,
454 doi:10.1029/2000JD900287.

455 Grutter, M., Glatthor, N., Stiller, G. P., Fischer, H., Grabowski, U., Höpfner, M., Kellmann, S.,
456 Linden, A., and von Clarmann, T. (2010), Global distribution and variability of formic acid as
457 observed by MIPAS-ENVISAT, *Journal of Geophysical Research*, 115, D10303,
458 doi:10.1029/2009JD012980.

459 González Abad, G., Bernath, P. F., Boone, C. D., McLeod, S. D., Manney, G. L., and Toon, G.
460 C. (2009), Global distribution of upper tropospheric formic acid from the ACE-FTS,
461 *Atmospheric Chemistry and Physics*, 9, 8039–8047, doi:10.5194/acp-9-8039-2009.

462 Hurtmans, D., Coheur, P.-F., Wespes, C., Clarisse, L., Scharf, O., Clerbaux, C., Hadji-Lazaro, J.,
463 George, M., and Turquety, S. (2012), FORLI radiative transfer and retrieval code for IASI,
464 *Journal of Quantitative Spectroscopy and Radiative Transfer*, 113, 1391–1408,
465 https://doi.org/10.1016/j.jqsrt.2012.02.036.

466 Hersbach, H., Bell, B., Berrisford, P., Hirahara, S., Horányi, A., Muñoz-Sabater, J., Nicolas, J.,
467 Peubey, C., Radu, R., Schepers, D., Simmons, A., Soci, C., Abdalla, S., Abellan, X., Balsamo,
468 G., Bechtold, P., Biavati, G., Bidlot, J., Bonavita, M., De Chiara, G., Dahlgren, P., Dee, D.,
469 Diamantakis, M., Dragani, R., Flemming, J., Forbes, R., Fuentes, M., Geer, A., Haimberger, L.,
470 Healy, S., Hogan, R. J., Hólm, E., Janisková, M., Keeley, S., Laloyaux, P., Lopez, P., Lupu, C.,
471 Radnoti, G., de Rosnay, P., Rozum, I., Vamborg, F., Villaume, S., and Thépaut, J. N. (2020),
472 The ERA5 global reanalysis, *Quarterly Journal of the Royal Meteorological Society*, 146, 1999–
473 2049, https://doi.org/10.1002/qj.3803.

474 Keene, W. and Galloway, J. (1984), Organic acidity in precipitation of North America,
475 *Atmospheric Environment*, 18, 2491–2497.

476 Keene, W. C. and Galloway, J. N. (1988), The biogeochemical cycling of formic and acetic acids
477 through the troposphere: An overview of current understanding, *Tellus B*, 40, 322–334.

478 Kawamura, K., Ng, L. L., and Kaplan, I. R. (1985), Determination of or- ganic acids (C1-C10) in
479 the atmosphere, motor exhausts, and engine oils, *Environmental Science and Technology*, 19,
480 1082–1086.

481 Lasko, K., Vadrevu, K.P., Tran, V.T., Ellicott, E., Nguyen, T.T., Bui, H.Q. and Justice, C.
482 (2017), Satellites may underestimate rice residue and associated burning emissions in Vietnam.
483 *Environmental Research Letters*, 12(8), p.085006.

Li, L., Ni Z., Qi, C., Yang, L., Han, C. (2022), Pre-Launch Radiometric Calibration of Geostationary Interferometric Infrared Sounder on FengYun-4B Satellite, *Acta Optica Sinica*, 42(6).

Li, P., Feng, Z., Jiang, L., Liao, C. and Zhang, J. (2014), A review of swidden agriculture in Southeast Asia. *Remote Sensing*, 6(2), pp.1654-1683.

Millet, D. B., Baasandorj, M., Farmer, D. K., Thornton, J. A., Baumann, K., Brophy, P., Chaliyakunnel, S., de Gouw, J. A., Graus, M., Hu, L., Koss, A., Lee, B. H., Lopez-Hilfiker, F. D., Neuman, J. A., Paulot, F., Peischl, J., Pollack, I. B., Ryerson, T. B., Warneke, C., Williams, B. J., and Xu, J. (2015), A large and ubiquitous source of atmospheric formic acid, *Atmospheric Chemistry and Physics*, 15, 6283–6304, https://doi.org/10.5194/acp-15-6283-2015.

Paulot, F., Wunch, D., Crounse, J. D., Toon, G. C., Millet, D. B., DeCarlo, P. F., Vigouroux, C., Deutscher, N. M., González Abad, G., Notholt, J., Warneke, T., Hannigan, J. W., Warneke, C., de Gouw, J. A., Dunlea, E. J., De Mazière, M., Griffith, D. W. T., Bernath, P., Jimenez, J. L., and Wennberg, P. O. (2011), Importance of secondary sources in the atmospheric budgets of formic and acetic acids, *Atmospheric Chemistry and Physics*, 11, 1989–2013, doi:10.5194/acp-11-1989-2011.

Pommier, M., Clerbaux, C., Coheur, P.-F., Mahieu, E., Müller, J.-F., Paton-Walsh, C., Stavrakou, T., and Vigouroux, C. (2016), HCOOH distributions from IASI for 2008–2014: comparison with ground-based FTIR measurements and a global chemistry-transport model, *Atmospheric Chemistry and Physics*, 16, 8963–8981, https://doi.org/10.5194/acp-16-8963-2016.

Pommier, M., Clerbaux, C., and Coheur, P.-F. (2017), Determination of enhancement ratios of HCOOH relative to CO in biomass burning plumes by the Infrared Atmospheric Sounding Interferometer (IASI), *Atmospheric Chemistry and Physics*, 17, 11089–11105, https://doi.org/10.5194/acp-17-11089-2017.

Razavi, A., Karagulian, F., Clarisse, L., Hurtmans, D., Coheur, P. F., Clerbaux, C., Müller, J. F., and Stavrakou, T. (2011), Global distributions of methanol and formic acid retrieved for the first time from the IASI/MetOp thermal infrared sounder, *Atmospheric Chemistry and Physics*, 11, 857–872, doi:10.5194/acp-11-857-2011.

R'Honi, Y., Clarisse, L., Clerbaux, C., Hurtmans, D., Duflot, V., Turquety, S., Ngadi, Y., and Coheur, P.-F. (2013), Exceptional emissions of NH_3 and HCOOH in the 2010 Russian wildfires, *Atmospheric Chemistry and Physics*, 13, 4171–4181, doi:10.5194/acp-13-4171- 2013.

Roberts, G., Wooster, M. & Lagoudakis, E. (2009), Annual and diurnal African biomass burning temporal dynamics. *Biogeosciences* 6, 849–866.

Rodgers, C. D. (2000), Inverse Methods for Atmospheric Sounding: Theory and Practice, World Scientific, Singapore.

Stavrakou, T., Müller, J.-F., Peeters, J., Razavi, A., Clarisse, L., Clerbaux, C., Coheur, P.-F., Hurtmans, D., Mazière, M. D., Vigouroux, C., Deutscher, N. M., Griffith, D. W. T., Jones, N.,

522 and Paton-Walsh, C. (2012), Satellite evidence for a large source of formic acid from boreal and
523 tropical forests, *Nature Geoscience*, 5, 26–30.

524 Yang, J., Zhang, Z., Wei, C., Lu, F., and Guo, Q. (2017), Introducing the new generation of
525 Chinese geostationary weather satellites, Fengyun-4, *Bulletin of the American Meteorological*
526 *Society*, 98, 1637–1658, https://doi.org/10.1175/BAMS-D-16-0065.1.

527 Zeng, Z.-C., Lee, L., and Qi, C. (2023a) Diurnal carbon monoxide observed from a geostationary
528 infrared hyperspectral sounder: first result from GIIRS on board FengYun-4B, *Atmospheric*
529 *Measurement Techniques*, 16, 3059–3083, https://doi.org/10.5194/amt-16-3059-2023.

530 Zeng, Z.-C., Lee, L., Qi, C., Clarisse, L., and Van Damme, M. (2023b), Optimal estimation
531 retrieval of tropospheric ammonia from the Geostationary Interferometric Infrared Sounder on
532 board FengYun-4B, *Atmospheric Measurement Techniques*, 16, 3693–3713,
533 https://doi.org/10.5194/amt-16-3693-2023.